THE ALTERATION OF MECHANICAL BEHAVIOR FOR $Ba_{0.5}Sr_{0.5}Fe_{12}O_{19}/(Ni_{0.5}Zn_{0.5})Fe_2O_4$ NANOCOMPOSITES

MALAK YASSINE[1], NOUR EL GHOUCH[2,*],
A. M. ABDALLAH[1], KHULUD HABANJAR[1], R. AWAD[1,3]

[1]Physics Department, Faculty of Science, Beirut Arab University, 11-5020, Beirut, Lebanon
[2]Chemistry Department, Faculty of Science, Beirut Arab University, 11-5020, Beirut, Lebanon
[3]Physics Department, Faculty of Science, Alexandria University, 21511, Alexandria, Egypt
*Corresponding Author: n.ghosh@bau.edu.lb

Abstract

$Ba_{0.5}Sr_{0.5}Fe_{12}O_{19}/x(Ni_{0.5}Zn_{0.5})Fe_2O_4$ nanocomposites with x = 10, 20, 30, and 50 wt.% derived from nickel zinc ferrite added to barium strontium hexaferrite were synthesized and characterized in this work. The prepared nanoparticles and nanocomposites were manufactured by co-precipitation and high-speed ball milling approaches. FTIR spectroscopic analysis revealed the absorption peaks that are characterized of both soft spinel and hard hexagonal ferrites in the nanocomposites. Additionally, the mechanical parameters have been computed from the FTIR data. Besides, force constant on A-site and B-site, Debye temperature, longitudinal, transverse and mean elastic wave velocities of the prepared samples, have been calculated. Furthermore, Vickers microhardness (H_V) tests were made to analyse the mechanical properties of the prepared samples under a range of applied loads (0.49-9.8 N) and temperatures (30–80 °C). The H_V measurements revealed that the prepared samples exhibited the behaviour of normal indentation size effect. Diverse models were theoretically used to study the obtained H_V values. The most appropriate theoretical model to depict the actual H_V values is the modified proportional sample resistance model. Besides, with increasing temperature, the BaSr/10%NiZn sample had the highest H_V values among the nanocomposites.

Keywords: Co-precipitation method, Elastic modulus, Nanocomposites, Temperature, Vickers microhardness.

1. Introduction

The wide application of soft spinel and hard hexagonal ferrites in the permanent magnets and recording media industry [1], makes the nanocomposites one of the most promising candidate for future industrial investigations. Many literature reporting the optical, magnetic, and electrical properties of ferrite nanocomposites [2-4]. However, the mechanical properties for such type of these nanocomposites, which are related to the strength of these materials, have not yet been studied. The mechanical parameters of hard/soft ferrite nanocomposites must be determined to design and fabricate practical devices for applications such as magnetic media disk application [4].

Knowing the mechanical properties of ferrites is critical because these materials must be mechanically resistant to avoid the damage during component assembly and machining [5]. In addition, the mechanical properties of hexaferrites are significant and are affected by many manufacturing conditions including pressure, temperature and duration of sintering [6]. Hardness tests are often employed in industry to evaluate the usability of fabrication materials and, in particular, the control of heat treatment performance. In this regard, the Vickers microhardness test is a preferred method for estimating the mechanical properties of hard/soft ferrite nanocomposites. Besides, nanoparticle inclusion has demonstrated their efficiency in improving the mechanical characteristics and mechanical parameters of composites [7]. The wet chemical co-precipitation approach has surpassed other preparation methods for the synthesis of nanocomposites since it is easy, affordable, and practical for large-scale production [8].

Vickers microhardness test was performed on many composites such as Tokunaga et al. [9] reported that the carbon nanotubes and fullerenes, were created via a procedure of extreme plastic deformation by high pressure torsion. Vickers microhardness was over 120 H_V and grain size with 5 mass% of fullerene was decreased to $\sim$ 80 nm, while the grain size without fullerenes is $\sim$500 nm. Also, it is expected that the fullerenes would be distributed unevenly throughout the aluminum composites, which is consistent with their mechanical characteristics. Moreover, Farhat et al. [10] studied the mechanical characteristics of zinc erbium oxide at different applied loads and dwell times. The load independent microhardness data of erbium doped zinc oxide nanoparticle samples were revealed to be best considered by the modified proportional specimen resistance model. Furthermore, Joshua et al. [11] fabricated AA7068/TiO_2 metal matrix composite via powder metallurgy technique. They found that the inclusion of TiO_2 particles increased the microhardness of the composites.

To the best of our knowledge, no prior literature studied experimentally the effect of the addition of $(Ni_{0.5}Zn_{0.5})Fe_2O_4$ (C_0) to the $Ba_{0.5}Sr_{0.5}Fe_{12}O_{19}$ (C_1) nanoparticles on the mechanical characteristics of the prepared nanocomposites. As previously reported in our work [12], C_1, C_0 nanoparticles, and C_1/xC_0 nanocomposites, with 4 different ratios of 100:10, 100:20, 100:30, and 100:50, were prepared by the co-precipitation and high-speed ball milling methods, respectively. C_1 and C_0 were found to be the two primary phases of nanocomposites, according to XRD studies. Also, C_1 and C_0 had hexagonal and spherical morphologies, respectively, according to the TEM investigation. The addition of C_0 reduces the nanocomposites' size. In addition, the magnetic investigation revealed a majority of dipolar interactions with the C_0 addition. When

compared to C_1, the $(BH)_{max}$ of the nanocomposite with 10% of NiZn improved by 10%, reaching a maximum value of 22.89 kJ/m^3. These prepared samples were recognized as promising permanent magnet candidates.

In the current work, (C_1), (C_0) nanoparticles, and C_1/xC_0 nanocomposites, with x = 10, 20, 30 and 50 wt.%, which are denoted as $C_{1.1}$, $C_{1.2}$, $C_{1.3}$ and $C_{1.5}$, respectively, were prepared via the co-precipitation and high-speed ball milling methods. C_1 and C_0 were considered as hard and soft magnetic materials. The elastic properties were estimated by Fourier transform infrared spectroscopy. Also, the Vickers microhardness analysis has been carried out using several empirical and theoretical models with a dwell period of 30 s. The Vickers microhardness (H_V) results are analyzed using Meyer's law, Hays-Kendall approach, elastic/plastic deformation model, proportional specimen resistance model, and modified proportional specimen resistance model. The best model for characterizing the Vickers microhardness of the prepared samples is also discussed. Additionally, the microhardness curves are used to estimate Vickers microhardness, Young's modulus, yield strength, and fracture toughness values. Besides, studying the effect of temperature on the mechanical properties of the prepared samples is another aim of this work.

2. Experimental

C_1 and C_0 nanoparticles and C_1/xC_0 nanocomposites were fabricated via the wet chemical co-precipitation and high-speed ball milling methods, as reported in our previous work [12].

The functional groups presented in the samples were studied using FTIR, via Nicolet iS5 spectrometer. Around 2 mg of each sample were finely combined with approximately 200 mg of KBr powder. The resulting powders were then made into a disc by pressing it in a mechanical pellet presser, where the pressure was maintained for several minutes before removing the formed KBr disk. The disc is then ready for scanning, while 100 % KBr disc was also prepared for use as the background.

The mechanical properties were performed at room temperature with a digital microhardness tester (MHVD-1000IS). Around 2 g of each sample was pressed into a disc sintered at 1000 °C for 4 h. The applied static loads were 0.49 - 9.8 N throughout the measurements, and a dwell period of 30 s. In addition, the prepared samples are exposed to heat-treatment at different temperatures (30 - 80 °C) with applied static load of 500 N and a dwell period of 30 s.

3. Theoretical Approach

3.1. FTIR

An FTIR spectrometer continuously records high spectral resolution data over a wide spectral range. It offers a considerable advantage over dispersed spectrometers, which can only determine intensity over a small number of wavelengths at a time. The chemical bonding, metal-oxygen vibration positioning modes, and elastic parameters of ferrites are all determined from the FTIR data analysis. The FTIR absorption spectra of ferrites are intensely reliant on the distribution of various cations in tetrahedral (A sites) and octahedral (B sites) of the spinel and hexagonal lattices [13]. According to Waldron [14], the higher frequency absorption band (v_1) is affected by stretching vibrations of the bond between the

cation in the tetrahedral site and oxygen, while the lower frequency absorption band (v_2) is resulted by vibrations of the bond between the cation in the octahedral site and oxygen. The variation in band position (v_1 and v_2) is due to the distance between the O^{2-} and Fe^{3+} ions in both octahedral and tetrahedral sites. In tetrahedral coordination, Fe^{3+} and O^{2-} are closer together, resulting in a stronger covalent bond.

The following equations are used to compute the tetrahedral (corresponds to A site) force constant, denoted as k_t, and the octahedral (corresponds to B site) force constant, denoted as k_o, by considering the positions of high (v_1) and low frequency (v_2) absorption band in the infrared spectrum [15].

$$k_t = 4\pi^2 {v_1}^2 c^2 \mu_m, \tag{1}$$

$$k_o = 4\pi^2 {v_2}^2 c^2 \mu_m, \tag{2}$$

here the force constant and speed of light (2.99×10^8 ms^{-1}) are k and c, respectively. The band frequency of A/B sites in cm^{-1} is represented by v. The reduced mass for the Fe^{3+} ions and the O^{2-} ions ($\sim 2.061 \times 10^{-23}$ g) is denoted by μ_m [15].

The Debye temperature (θ_D) is a basic property of solids that relates elastic and thermodynamic characteristics such as specific heat, which is calculated from this relationship proposed by Anderson [16]:

$$\theta_D = \frac{hcv_{av}}{2\pi k_B} = 1.438 v_{av}, \tag{3}$$

where Boltzmann's and Planck's constants are k_B and h, respectively, the speed of light is c. As a result, in ferrite materials the value of $\frac{hC}{2\pi k_B} = 1.438$ [16]. Also, v_{av} is the average value of the wavenumbers which is equal to $(v_1 + v_2)/2$ for the ferrites.

The average force constant is obtained using the expression:

$$k_{av} = \frac{k_t + k_o}{2}, \tag{4}$$

The study of elastic properties is significant because it defines the binding force strength of a ferrite material and also helps to reduce the mechanical straining of these materials during manufacturing and industrial use [17]. FTIR and XRD analyses are employed to determine the elastic property of ferrite materials [18]. The stiffness constant and other elastic parameters are calculated using force constants derived from infrared spectra and crystallographic parameters. According to Waldron [14], stiffness constant $C_{11} = C_{12}$ for the materials possessing the cubic spinel crystal structure. Moreover, the materials possessing the hexagonal crystal structure contain five stiffness constants i.e. C_{11}, C_{12}, C_{13}, C_{33}, and C_{44}. Because it is assumed that hexagonal crystals are elastically isotropic, thus, $C_{11} = C_{13}$, $C_{12} = C_{13}$, and $C_{44} = 1/2 (C_{11} - C_{12})$ [19]. Stiffness constants C_{11} and C_{12} are given by the equations [20]:

$$C_{11} = \frac{k_{av}}{a}, \tag{5}$$

$$C_{12} = \frac{C_{11}\sigma}{1-\sigma}, \tag{6}$$

where a denotes the lattice constant and σ represents poison ratio respectively. Poison's ratio is calculated by the equation $\sigma = 0.324 (1 - 1.043P)$ in which P

is the porosity of the prepared samples. The x-ray density (ρ_x) for the prepared samples has been computed using the following equation [20]:

$$\rho_x = \frac{Z \times M}{N V_{cell}^3},$$ (7)

where the Avogadro's number (6.023×10^{23} atom/mole) is N, the molar mass of the sample is M, number of molecules per unit cell is Z (for spinel ferrites $Z = 8$ and for hexaferrites $Z = 2$), and the unit cell volume is V_{cell}.

The bulk density ρ_B for the prepared samples has been calculated by the following equation [21]:

$$\rho_B = \frac{m}{\pi r^2 h},$$ (8)

where the mass, radius and thickness are m, r and h, respectively, of each pellet of the prepared samples.

The porosity (P) of the prepared samples attained from the values of the ρ_x and ρ_B by the following equation [21]:

$$P = 1 - \frac{\rho_B}{\rho_x},$$ (9)

Other elastic moduli for the prepared samples are computed using the following relations [20]:

Elastic's modulus (GPa): $E = \frac{(C_{11} - C_{12})(C_{11} + 2C_{12})}{(C_{11} + C_{12})},$ (10)

Rigidity modulus (GPa): $G = \frac{E}{2(\sigma + 1)},$ (11)

Bulk modulus (GPa): $K = \frac{1}{3}(C_{11} + 2C_{12}),$ (12)

The X-ray density ρ_x and stiffness constant (C_{11}) are used to calculate the longitudinal elastic wave velocity (V_l) and transverse wave velocity (V_t) by the following equations [22]:

$$V_l = \sqrt{\frac{C_{11}}{d_{XRD}}},$$ (13)

$$V_t = \frac{V_L}{\sqrt{3}},$$ (14)

The mean elastic wave velocity (V_m) can be estimated using the longitudinal wave velocity (V_l) and transverse wave velocity (V_t) in the following equation [23]:

$$V_m = \left[3 \left(\frac{V_l^3 \times V_t^3}{V_t^3 + 2V_l^3} \right) \right]^{1/3}$$ (15)

3.2. Vickers microhardness

The hardness of the prepared samples is determined by measuring the resistance that appears when a stiff (diamond) indenter is immersed in the sample's surface. The indentation process is divided into two steps: loading by exerting an applied load for a few seconds and unloading. After that, the indenture's permanent impression is obtained, and the diagonals (d_1 and d_2) of the indentation were

measured using a calibrated microscope. Then, the average diagonal length of the indentation (d) is calculated in micrometers according to this equation:

$$d = \frac{d_1 + d_2}{2}, \tag{16}$$

Hence, the load-dependent microhardness was estimated using the relationship [24]:

$$H_V = \frac{2F\sin\frac{\alpha}{2}}{d^2} \approx 1854.4 \times \frac{F}{d^2} \text{ (GPa)}, \tag{17}$$

where the applied static load is symbolized by F in Newton and the face angle of $136°$ is signified by α for the indenter.

3.2.1. Modelling

3.2.1.1. Meyer's law

Meyer's law, which is used to determine the behaviour of the material, it is the simplest approach to explain the trend of the indentation size effect (ISE) or reverse ISE ($RISE$) behaviour of materials. It relates the static applied load (F) and diagonal length (d) of the indentation [25]:

$$F = Ad^n, \tag{18}$$

where the typical microhardness constant is A and a Meyer's index is the exponent n which describes the ISE. The material follows the $RISE$ behaviour when the n value is greater than 2. In contrast, the material displays the ISE behaviour if the n value is lower than 2. Furthermore, it is widely known that the Kick's law is effective when the n value equals 2, which means that the hardness is independent to the applied load and given as follows: $F = A_{1k}d^n$.

3.2.1.2. Hays-Kendall (HK) model

The ISE behaviour observed in the microhardness tests is achieved by Hays-Kendall (HK) model for a variety of materials [26]. This model claims that the minimum load (W) is necessary to produce plastic deformation and below in which only an elastic deformation is visible at H_V levels, which is a sample resistance pressure. The indenter can enter the material beyond a particular load value known as the critical applied load value. As a result, the indentation size begins to rise after the material's critical applied load value that is proportional to an effective load $F_{eff} = F - W$ rather than the applied load, as shown by the following relation:

$$F - W = A_1d^2, \tag{19}$$

where the load-independent microhardness constant is denoted by A_1. The values of W and A_1 are obtained from F to d^2 graph for all the prepared samples. In addition, due to HK approximation, the HK microhardness (H_{HK}) and the HK load-independent microhardness (H_{HKin}) can be expressed using the following equations, respectively:

$$H_{HK} = 1854.4 \times \frac{F-W}{d^2}, \tag{20}$$

$$H_{HKin} = 1854.4 \times A_1 \tag{21}$$

3.2.1.3. Elastic-plastic deformation (EPD) model

Indentation load dependence was provided by Bull et al. [27] and Upit et al. [28] by including an elastic component (d_0) into the observed plastic indentation semidiagonal (d) by the equation [29]:

$$F = A_2(d + d_0)^2, \tag{22}$$

where the real microhardness constant is A_2, from which the EPD microhardness (H_{EPD}) and the EPD load-independent microhardness (H_{EPDin}) are calculated according to the following equations, respectively:

$$H_{EPD} = 1854.4 \times \frac{F}{(d+d_0)^2}, \tag{23}$$

$$H_{EPDin} = 1854.4 \times A_2 \tag{24}$$

3.2.1.4. Proportional sample resistance (PSR) model

PSR model can characterize the *ISE* behaviour for various materials, as reported by Li and Bradt [30]. Also, PSR model is considered as the alteration of HK model by replacing W in Eq. (19) by the term $\alpha_1 d$ as the following relation:

$$F = \alpha_1 d + \beta d^2, \tag{25}$$

where the surface energy and the true microhardness coefficient are represented by α_1 and β [30]. These two terms can be used to calculate the PSR microhardness (H_{PSR}) and the PSR load-independent microhardness (H_{PSRin}) and they are given by the following equations, respectively:

$$H_{PSR} = 1854.4 \times \frac{\alpha_1 d + \beta d^2}{d^2}, \tag{26}$$

$$H_{PSRin} = 1854.4 \times \beta, \tag{27}$$

3.2.1.5. Modified proportional sample resistance (MPSR) model

When the impact of machining-induced plastically deformed surface on microhardness testing is considered, the PSR model is modified using Eq. (28) [31]:

$$F = \alpha_2 + \alpha_3 d + \alpha_4 d^2, \tag{28}$$

where the constant α_2 signifies the minimum applied load for the impression length, and it is the same to the load independent constant (W) in the HK model. Moreover, the constants α_3 and α_4 are equivalent to α_1 and β in the PSR model. The MPSR microhardness (H_{MPSR}) and the MPSR load-independent microhardness (H_{MPSRin}) can be estimated according to the following equations, respectively:

$$H_{MPSR} = 1854.4 \times \frac{\alpha_2 + \alpha_3 d + \alpha_4 d^2}{d^2}, \tag{29}$$

$$H_{MPSRin} = 1854.4 \times \alpha_4 \tag{30}$$

The following equations can be used to calculate the elastic modulus (E_m), yield strength (Y), fracture toughness (K_f), and the brittle index (B_i) values based on the microhardness:

$$H_V = \frac{1}{20} E_m (1 - 1.9P + 0.9P^2), \tag{31}$$

$$Y \approx \frac{H_V}{3}, \tag{32}$$

$$K_f = \sqrt{2E\alpha_1}, \tag{33}$$

$$B_i = \frac{H_V}{K_f}. \tag{34}$$

4. Results and Discussion

4.1. FTIR

The prepared materials' FTIR spectra are recorded in the range 4000 to 400 cm^{-1}, as shown in Fig. 1(a). The absorption band around 3426-3445 cm^{-1} is ascribed to the intermolecular hydrogen bond of v(O-H, stretch) [32]. The adsorption band at 1624-1642 cm^{-1} correspond to the bending mode of water molecules absorbed during sample preparation process δ(H-O-H, bend) [33]. The other absorption bands at 2340-2367 cm^{-1} originate from axial symmetrical deformation of CO_2 of v_s(C=O, stretch) [33]. Besides, the FTIR spectra in the range of 400-700 cm^{-1} of the prepared samples deconvoluted, to determine their absorption bands in Fig. 1(b). There are clear three principle absorption bands for C_1 and the nanocomposites and two principle absorption band for C_0 recorded in the range of 600-400 cm^{-1} in the infrared spectra. A high vibration band between v_1(539-602 cm^{-1}) corresponds to the tetrahedral A site metal-oxygen bonding of Fe-O bending by Fe-O_4 and a low vibration band in the range of v_2(400-443 cm^{-1}) attributes to the octahedral B site metal-oxygen vibrations of Fe-O stretching of Fe-O_6 [34, 35]. The absorption frequency band for A and B sites are presented in Table 1. Because A sites have shorter bond lengths than B sites, the v_1(values are much greater than those of v_2 as seen in Table 1).

These bands exhibit a slight shift in frequency to high frequency at x = 20 wt.%. This is due to cation rearrangement between different sites of the C_1 and C_0 structures [36]. The band shift of the v_1 and v_2 frequencies shows a change in the force constant, because the vibration frequency is related to the force constant (K). Table 1 lists the computed values of the force constants k_t and k_o for A and B sites, respectively. It is shown that the force constants of the k_t and k_o increase with the addition of C_0 up to x = 20 wt.%. This rise in the force constants is due to an increase in the vibrating frequency of the tetrahedral and octahedral sites, as a result of shortening the bond length [37]. Conversely, the force constants k_t and k_o decrease with further additions of C_0, exhibiting the same pattern as the absorption frequencies (v_1 and v_2) [37]. Due to this decrease in force constants, as interatomic separation rises, the bonds at the octahedral and tetrahedral sites become weaker [38].

The variation in Debye temperature θ_D for the prepared samples can be noticed in Table 1. It is shown that θ_D decreases from pure BaSr to x = 10 wt.%, then increases up to a maximum value at x = 20 wt.% and slowly decreases thereafter. The theory of specific heat can be explained this shift in Debye temperature [39]. This theory states that when θ_D drops, the electrons absorb some of the heat, proving that electrons are responsible for the conduction for these samples to become n-type. On the other hand, the abrupt increase in θ_D may indicate a transformation in sample conductivity from conduction electrons (n-type) to holes (p-type) with the addition of $NiZn$ up to 20 wt.%. Additionally, the elevated Debye

temperature may influence by the elevated rigidity at x = 20 wt.% and then decreases with further additions [40].
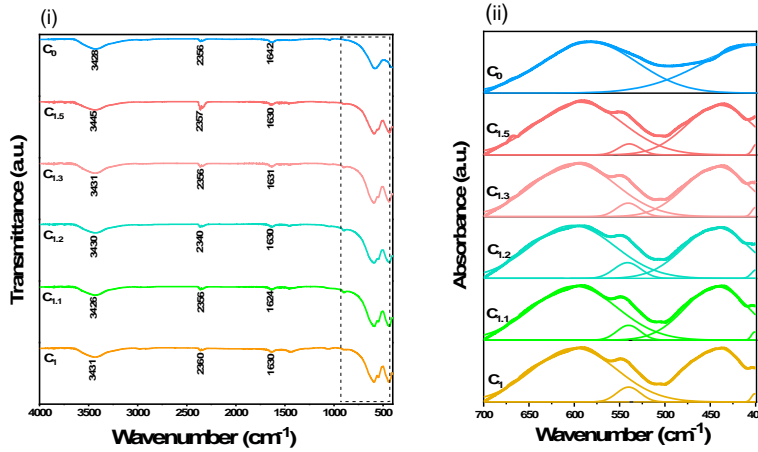

Fig. 1. (a) Full range FTIR spectra and (b) the deconvoluted spectra in the fingerprint region for the prepared samples.

Table 1. Vibrational band frequencies (v_1 and v_2), force constants (k_t, k_o, and k_{av}), X ray densities (ρ_x), bulk densities (ρ_B), Porosities (P), Debye temperature (θ_D) and Poisson's ratio (σ).

x (wt.%)	C_1	C_0	C_{1.1}	C_{1.2}	C_{1.3}	C_{1.5}
v_1 (GPa)	599	583	598	602	600	594
v_2 (GPa)	443	394	442	443	442	439
k_t (GPa)	262.99	249.13	262.11	265.63	263.87	258.62
k_o (GPa)	143.84	113.78	143.19	143.84	143.19	141.26
k_{av} (GPa)	203.42	181.45	202.65	204.74	203.53	199.94
ρ_x (g/cm³)	5.22	5.38	5.34	5.44	5.56	5.83
ρ_B (g/cm³)	2.87	4.38	3.65	2.96	1.17	1.97
P (g/cm³)	0.45	0.19	0.32	0.46	0.79	0.66
θ_D (K)	749.198	702.463	747.760	751.355	749.198	742.727
σ (GPa)	0.17	0.26	0.22	0.17	0.06	0.10

The variation of ρ_x, with C_0 concentration has been adduced also in Table 1. The value of ρ_x rises with the addition of C_0. This behavior is explained by the

decrease in the unit cell volume of the prepared samples as the unit cell volume is inversely proportional to X-ray density. Moreover, the values of ρ_B are less than that of ρ_x as seen in Table 1, owing to the presence of inter and intra granular porosity created during sintering process [41]. The porosity is found to increase from pure BaSr to $x = 20$ wt.%, then increases up to a maximum value at $x = 30$ wt.% and decreases with further addition. This behavior is recognized to the irregular shape of grain size in the prepared samples. In addition, the decreasing trend in porosity indicates that some densification existed in case of $C_{1.1}$ and $C_{1.5}$, that is owing to increase in bulk density in these samples [42].

The obtained values of Poisson's ratio σ exhibit nonlinear behavior with the addition of C_0 (in the range of 0.06-0.26) as illustrated in Table 1. The obtained values of σ lie in the range from -1 to 0.5 which is in agreement with the theory of isotropic elasticity [43].

Figure 2(a) shows the variation of stiffness constants, C_{11} and C_{12}, as function of concentration of C_0. The rise in C_{11} and C_{12} is attributed to the loss of retained water from the samples with the addition of C_0, but the abrupt decline can be attributed to the transformation process, in which the unit cell volume rises rapidly. However, stiffness constant, C_{11} and C_{12} are determined by atomic bonding tightness and force constant, therefore their decline may be related to weak atomic bonding between Ba^{2+}, Sr^{2+}, Ni^{2+}, Ni^{3+}, Zn^{2+}, Fe^{2+}, and Fe^{3+} cations as the addition of C_0 increases.

The variation of elastic moduli: Young's modulus (E), rigidity modulus (G) and bulk modulus (K) against the concentration of C_0 is presented in Fig. 2(b). It is seen that the elastic moduli drop, indicating that the inter-atomic bonding between distinct atoms in the crystal lattice weakens with the addition of C_0 [43]. The increase in cation repulsion between electrons with the addition of C_0, resulting in a drop in elastic moduli. In contrast, the increase in the elastic moduli is due to the cations being rearranged within the crystal lattice, which will enhance crystallization process [44]. Consequently, the strength of the bonding between the corresponding ions increases.
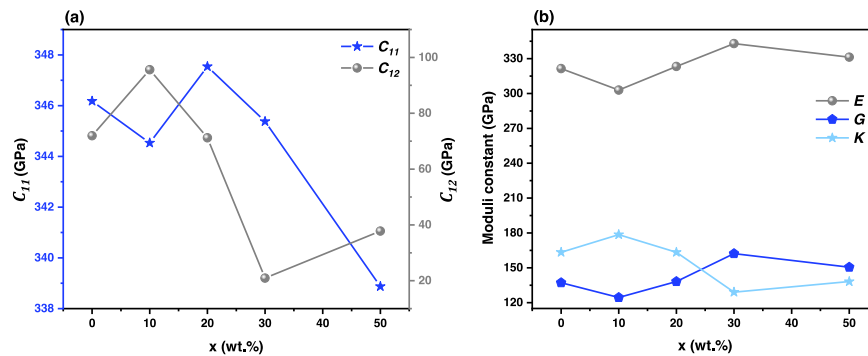

Fig. 2. Variation of , C_{11} (a) and C_{12} and (b) elastic moduli constants as a function of composition x.

The variation of longitudinal wave velocity (V_l), transverse wave velocity (V_t) and the mean elastic wave velocity (V_m) of the prepared samples are shown in Fig.

3. The decrease in velocities may be related to decrease in force constant. The consistent finding for all ferrites is that transverse wave velocities (V_t) has lesser values than longitudinal wave velocity (V_l) [45].
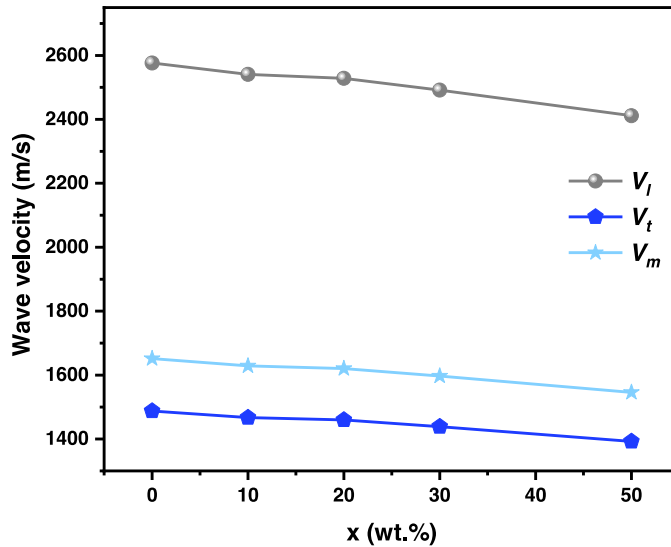

Fig. 3. Variation of (V_l), (V_t) and (V_m) as a function of composition x.

4.2. Vickers Microhardness

The Vickers microhardness H_V was calculated according to eq. (17) and plotted as a function of the applied load for the prepared samples in Fig. 4. As the applied load rises up to 2.94 N, H_V drops quickly (a load dependent segment), after that H_V achieves saturation, which is nearly the plateau region, for higher loads $F > 2.94$ N (a load independent segment). This decrease in H_V values is known as the indentation size effect (*ISE*). Because the material has weak grain boundaries and the indenter mainly touches the surface layers, H_V is large at low indentation loads [7]. Whereas the impact of the inner layers becomes more relevant as the indenter's penetration depth rises at higher applied loads. For that reason, H_V values remain almost constant as the applied load increases [10]. Additionally, the inset of Fig. 4 shows that H_V increases by adding *NiZn* up to $x = 20$ wt.% into BaSr for all applied loads (F). This enhancement is due to a decrease in porosity or resistance to fracture propagation inside the grains, as well as an increase in grain connectivity [46]. However, H_V decreases with further additions due to a growth in the grain boundary weak links, specimen cracking/porosity, and impurity phases [46].

Table 2 includes the fitting equations for all the prepared samples that describe the change of H_V with applied load using quadratic formulas. The variation of the F^2 coefficients increases from 0.00171 to 0.0189 with the addition of C_0 from 10 to 20 wt.%. This result is explained by the fact that there are less fractures and dislocations in these samples associated with rise in H_V values [46]. On the other hand, the variation of the F^2 coefficients decreases with further additions of C_0 up to 50 wt. %. This is attributed to the quick growth in fractures and dislocations in these samples [46].
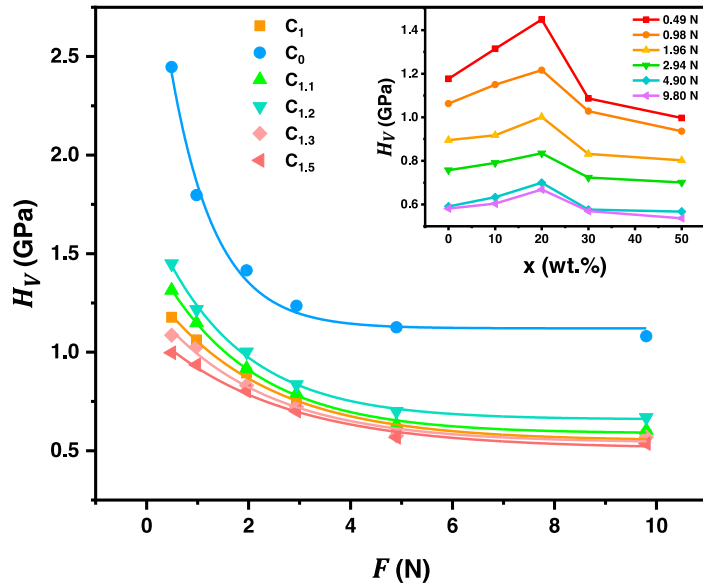
Fig. 4. Variation of experimental H_V as a function of the applied static load F for the prepared samples at a dwell time of 30 s. The inset shows the variation of , H_V with x for F = 0.49, 0.98, 1.96, 2.94, 4.90, and 9.80 N.

Table 2 Fitting parameters obtained from the theoretical models for the prepared samples.

x (wt.%)	C_1	C_0	$C_{1.1}$	$C_{1.2}$	$C_{1.3}$	$C_{1.5}$
Fitting relations	$H_V =$ 0.0144F² - 0.2106F + 1.262	$H_V=$ 0.0344F²- 0.4669F + 2.3904	$H_V=$ 0.0171F²- 0.2465F + 1.3863	$H_V=$ 0.0189F² - 0.2696F + 1.5034	$H_V=$ 0.0131F² - 0.1906F + 1.1794	$H_V=$ 0.0101F² - 0.1534F + 1.0702
R^2	1	0.863	0.982	0.969	0.994	0.999
H_V (GPa)	0.586	1.103	0.618	0.684	0.573	0.552
H_{HKin} (GPa)	0.549	1.037	0.571	0.636	0.541	0.512
H_{EPRin} (GPa)	0.463	0.890	0.482	0.538	0.464	0.445
H_{PSRin} (GPa)	0.433	0.831	0.447	0.501	0.434	0.419
H_{MPSRin} (GPa)	0.602	1.113	0.630	0.697	0.588	0.565

Several theoretical models are applied to determine the true microhardness or load-independent microhardness, which is the change of H_V with the applied static load F in the plateau limit regions. So, the relationships between the applied load and the indentation diagonal length are given below to characterize the *ISE* behavior of the prepared samples.

The $lnF - lnd$ graphs of the prepared samples are shown in Fig. 5, in which n values, that are obtained from the slope of the linear plot, are found to be less than 2

for each sample, verifying normal *ISE* behavior. The vertical intercept of the graph indicates A value, and the n and A values are summarized in Table 3. Furthermore, normal *ISE* behavior is considered to be correlated to geometrically necessary dislocations (GNDs). Consequently, this behavior can be explained as the prepared samples have high hardness under low loading conditions. As a result, the dislocations are assumed to regulate the deformation of materials with lower n values more than those with higher n values [47]. As well, upon adding 10 wt.% of C$_0$ to C$_1$, the value of n decreases from 1.577 to 1.553, suggesting less lattice damage owing to the migration of Ni^{2+} and Zn^{2+} ions in C$_0$ into Ba^{2+} and Sr^{2+} ions in C$_1$ [10]. In contrast, the value of n increases from 1.553 to 1.623 with the addition of C$_0$ from 10 to 50 wt.%, indicating larger lattice damage. This can be due to the inclusion of larger amount of C$_0$ to C$_1$. It is also important to classify the hardness of these materials, if the value of n is between 1 and 1.6, the material is hard and if it is greater than 1.6, the material is soft [10]. Hence, all the prepared samples are classified as soft materials, except for C$_{1.5}$ is considered as hard material.

Figure 6 illustrates the linear fitting of F against d^2 for the prepared samples. These obtained values of load independent microhardness for all the samples are tabulated in Table 2. As seen from Table 3 the values of W are positive for all the prepared samples (exhibiting the normal *ISE* behavior) and are almost greater than the lowest applied load employed in this research (0.49 N). This means that the applied loads are strong enough to create elastic and plastic deformations [7], and that once the indenter is removed, an elastic relaxation occurs on the sample's surface. Further, the values of A_1 change in the same way as the variation of H_V with F with the addition of C$_0$, verifying the *ISE* trend [7]. The observed microhardness values in the plateau region (H_{HKin}) are found to be nearly close to the theoretical H_V data given in Table 2. The deviation between the true hardness and the calculated microhardness from HK model varies from 5.5 % to 7.6 %. As a result, the HK model is inapplicable to studying true microhardness behavior for the prepared samples.
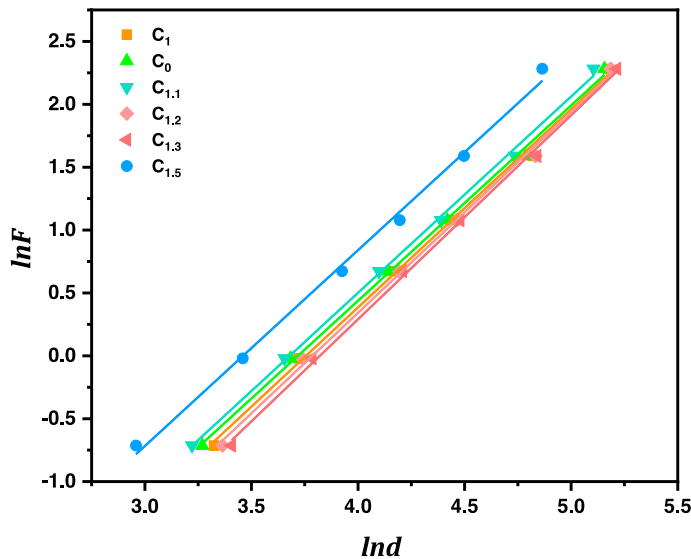

Fig. 5. lnF versus lnd for the prepared samples at a dwell time of 30 s.

**Table 3 Fitting relationship for H_V values with regard
to the applied test load; experimental and theoretical microhardness
analysis results for the prepared samples.**

| x (wt.%)			C_1	C_0	$C_{1.1}$	$C_{1.2}$	$C_{1.3}$	$C_{1.5}$
Meyer's parameters	n		1.577	1.557	1.553	1.561	1.598	1.623
	$A \times 10^{-3}$	(N/µm²)	2.681	4.575	3.106	3.206	2.361	2.03
HK's parameters	W	(N)	0.53	0.41	0.55	0.52	0.49	0.52
	$A_1 \times 10^{-4}$	(N/µm²)	2.96	5.59	3.08	3.43	2.92	2.76
EPD's parameters	$A_2 \times 10^{-3}$	(N/µm²)	0.25	0.48	0.26	0.29	0.25	0.24
	d_0	(µm)	20.61	12.91	20.85	18.89	19.45	19.64
PSR's parameters	$\alpha_1 \times 10^{-2}$	(N/µm)	1.341	1.596	1.426	1.429	1.235	1.18
	$\beta \times 10^{-4}$	(N/µm²)	2.34	4.48	2.41	2.70	2.34	2.26
MPSR's parameters	α_2	(N)	0.15	0.23	0.1	0.13	0.17	-0.01
	$\alpha_3 \times 10^{-2}$	(N/µm)	0.97	0.64	1.17	1.07	0.81	1.29
	$\alpha_4 \times 10^{-4}$	(N/µm²)	2.51	5.19	2.52	2.89	2.54	2.18
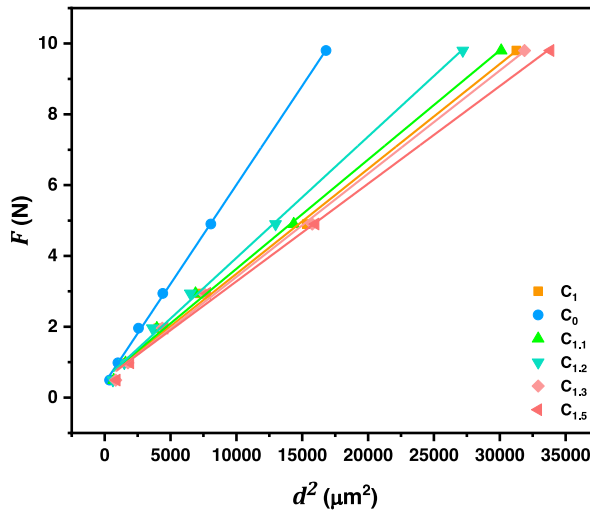
**Fig. 6. Effective load F as a function of d^2
for the prepared samples at a dwell time of 30 s.**

Figure 7 demonstrates the linear plot of $F^{0.5}$ versus d for the prepared samples. A_2 and d_0 are identified and Table 2 illustrates their findings. The results from the Hays-Kendall model are confirmed by the positive values of A_2 and d_0, which demonstrate that there is elastic deformation in the prepared samples along with plastic deformation, verifying the *ISE* behavior [10].

Table 3 clearly shows that the (H_{EPDin}) values are relatively away from the original microhardness values in the plateau region; hence, this model is insufficient in determining the actual hardness values for all the prepared samples. The deviation between the true microhardness and the calculated microhardness from EPD model varies from 19.0 % to 22.0 %.
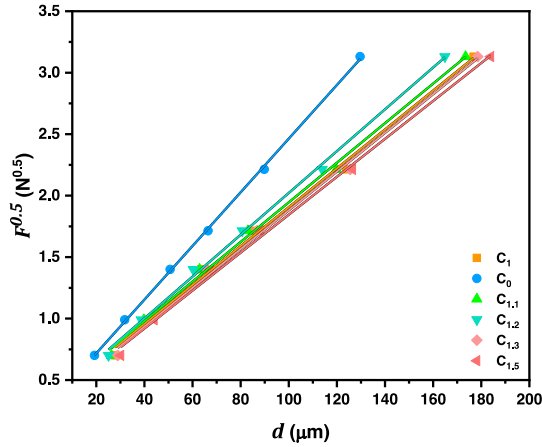
**Fig. 7. Linear plot of $F^{0.5}$ versus d for
the prepared samples at a dwell time of 30 s.**

Figure 8 depicts a plot of (F/d) versus d for the prepared samples, following PSR model. α_1 denotes the y-intercept and β denotes the slope, and their values are listed in Table 3. The tabulated data demonstrate that all the prepared samples exhibit positive values of α_1 and β, supporting the HK model results. These findings show the presence of elastic as well as plastic deformation, demonstrating *ISE* behavior in the prepared samples. Moreover, α_1 increases with the addition of C$_0$ up to 20 wt.% due to energy dissipation via fractures at the interfaces [7]. Furthermore, the sample transition values to the plateau differ from the load independent hardness values calculated using the PSR model. This demonstrates that this model is inadequate for identifying the true hardness levels in this investigation. The deviation between the true hardness and the calculated microhardness from PSR model varies from 24.1 % to 27.7 %.
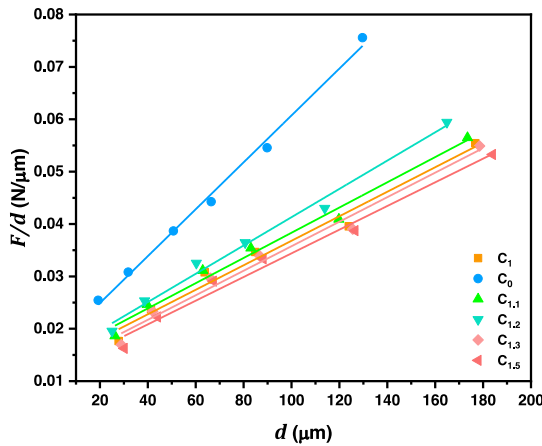

Fig. 8 . F/d versus d for the prepared samples at a dwell time of 30 s.

Figure 9 illustrates the change of F with d for the prepared samples. Table 3 provides the MPSR parameters α_2, α_3 and α_4, which are derived using a standard polynomial fit to the data. The positive values of α_2, describe that the samples suffer

from both elastic and plastic deformation. Furthermore, the experimental H_V values were quite close to the true microhardness values measured. The error between the true microhardness and calculated microhardness from MPSR model varies from 0.9% to 2.8%. As a result, the MPSR model is the most credible model for discussing the H_V findings and the mechanical properties of all the prepared samples in the plateau region. Moreover, the residual surface stress contribution of the MPSR model to the observed *ISE* behavior is negligible compared to the other models.
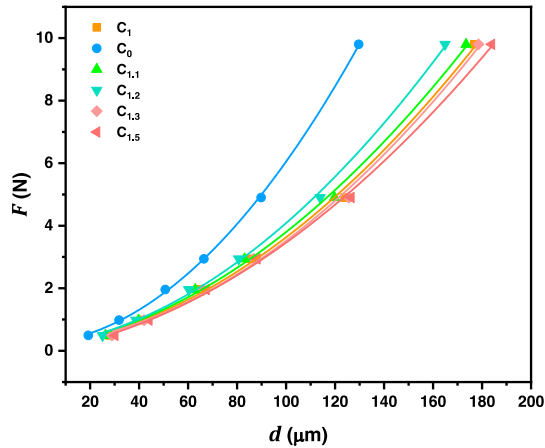

Fig. 9. *F* versus *d* for the prepared samples at a dwell time of 30 s.

Table 4 demonstrates the values of E_m, Y, k_f and B_i for the prepared samples. The values of E_m acquired from FTIR measurements are higher than those obtained from H_V measurements, but they follow a similar variation trend as shown in Fig. 10. This implies that the approach used to calculate elasticity parameters from FTIR measurements is accurate and acceptable. The values of E_m and Y change in the same trend of H_V owing to their dependency on the hardness. The elastic components' contribution to the fracture toughness (k_f) of nanocomposites with x = 10 and 20 wt.%, are comparatively larger than for nanocomposites with x = 30 and 50 wt.%, which results in a variation of their abilities to resist cracks (fracture behavior). So, the microstructure is important that can influence the fracture behavior [48]. Due to the inverse correlation between the fracture toughness and the ductility, samples with higher addition of C₀ show a higher ductility [48]. In addition, particle distribution have an impact on the ductility of the nanocomposites [49]. Furthermore, C₁.₂ has highest value of B_i, which has the most tendency to break when deformed. Moreover, because of the *ISE* behavior, the reduction of E_m, Y, and k_f values with applied load is also predicted.

Table 4 The calculated load-dependent H_V, E, Y, K_f, and B_i values for the prepared samples.

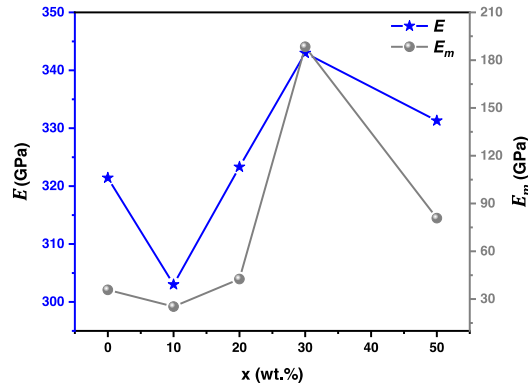| x (wt.%)	H_V (GPa)	E_m (GPa)	Y (GPa)	K_f (GPa/µm$^{1/2}$)	B_i (µm$^{1/2}$)
C₁	0.586	35.772	0.195	1.135	0.516
C₀	1.103	32.607	0.368	1.699	0.649
C₁.₁	0.618	25.263	0.206	1.202	0.514
C₁.₂	0.684	42.587	0.228	1.266	0.540
C₁.₃	0.573	188.373	0.191	1.077	0.532
C₁.₅	0.552	80.777	0.184	1.033	0.534

Fig. 10. Variation of *E* and *E$_m$* as a function of composition *x*.

Hardness measurements are performed on the prepared samples at 30, 40, 50, 60, 70 and 80 °C while keeping the dwell period constant at 30 s. Fig. 11 indicates that H_V values of C$_1$ and C$_0$ nanoparticles decline at higher temperature while H_V values remain almost similar for C$_1$/xC$_0$ nanocomposites. The increase in dislocation density (defects) results in a decrease in hardness as temperature increases [50]. From Fig. 11, the C$_{1.1}$ sample has the most enhanced H_V as temperature increases from 30 to 80 °C. This is due to the relatively uniform distribution of C$_0$ nanoparticles among the C$_1$ nanoparticles in C$_{1.1}$ sample [51]. This means that C$_{1.1}$ has less spaces between its nanoparticles at 80 °C [52]. C$_{1.1}$ sample shows the highest H_V values among the nanocomposites with increasing temperature, which is the most appropriate sample used in magnetic applications [53] as reported in our previous work [12].
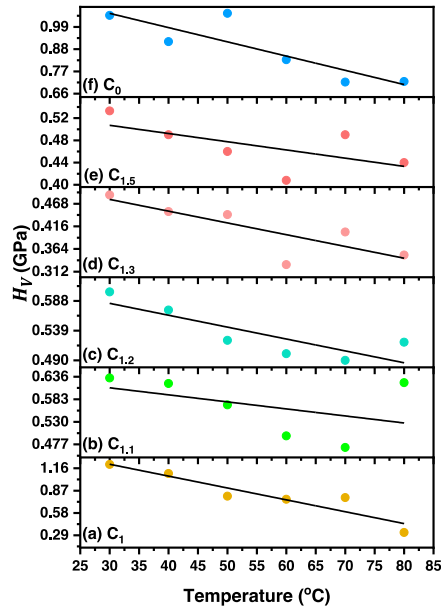

Fig. 11. *H$_V$* as a function of the temperature for the prepared samples with applied static load of 500 N and a dwell period of 30 s.

5. Conclusions

Magnetically hard/soft ferrite C_1/xC_0 nanocomposites with x = 10, 20, 30, and 50 wt.% have been prepared using the co-precipitation and high-speed ball milling techniques. FTIR spectroscopic analysis confirmed the purity of both spinel soft and hexagonal hard ferrites in the nanocomposites. The stiffness constant, elastic moduli and wave velocity values can be determined from FTIR. The H_V measurements revealed that the prepared samples exhibited the behaviour of normal indentation size effect. The H_V values improved with the addition of C_0 up to x = 20 wt.% for all applied loads (F), suggesting the decrease in porosity or resistance to crack propagation within the grains, and an increase strength of the bonds between the grains. Normal *ISE* behaviour was found when H_V declined as the applied load increased for all the prepared samples. Experimental results of H_V were examined using Meyer's law, HK approach, EPD model, PSR model and MPSR model. The MPSR model was the best in describing the actual microhardness values. However, the mechanical parameters E_m, Y, k_f and B_i for the prepared samples computed from H_V values performed to follow the same trend as H_V values with the addition of C_0. Further, the $C_{1.1}$ sample exhibited the greatest H_V values among the nanocomposites as temperature increased, confirming the relatively uniform distribution of C_0 nanoparticles into the BaSr nanoparticles.

Acknowledgments

Nomenclatures

B_i	Brittle index
E	Young's modulus from FTIR
E_m	Elastic modulus
G	Rigidity modulus from FTIR
H_{EPDin}	EPD Load-independent microhardness
H_{HKin}	HK Load-independent microhardness
H_{MPSRin}	MPSR Load-independent microhardness
H_{PSRin}	PSR Load-independent microhardness
H_V	Load-dependent microhardness
k	Force constant
K	Bulk modulus from FTIR
K_f	Fracture toughness
V_l	Longitudinal wave velocity
V_m	Mean elastic wave velocity
V_t	Transverse wave velocity
Y	Yield strength

Greek symbols

α_1	Surface energy
α_2	minimum applied load for the impression length
α_3	Surface energy

β	True microhardness coefficient
θ_D	Debye temperature
ρ_B	Bulk density
ρ_x	X-ray density
Abbreviations	
ISE	Indentation size effect behaviour
RISE	Reverse indentation size effect behaviour

References

1. Almessiere, M.A.; Slimani, Y.A.; Hassan, M.; Gondal, M.A.; Cevik, E.; and Baykal, A. (2021). Investigation of hard/soft $CoFe_2O_4/NiSc_{0.03}Fe_{1.97}O_4$ nanocomposite for energy storage applications. *International Journal of Energy Research*, 45(11), 16691-16708.

2. Mathews, S.A.; Babu, D.R.; Saravanan, P.; and Hayakawa, Y. (2020). Microwave absorption studies of $(Ba_{0.5}Sr_{0.5}Fe_{12}O_{19})_{1-x}/(NiFe_2O_4)_x$ hard/soft ferrite nanocomposites. *Materials Chemistry and Physics*, 252, 123063-123073.

3. Dhabekar, K.; and Mohan Kant, K. (2022). Soft/hard ferrite nanocomposites: Evaluation of temperature dependent dielectric properties. *Physica B: Condensed Matter*, 627, 413581-413588.

4. Matsumoto, M.; Morisako, A.; and Takei, S. (2001). Characteristics of Ba-ferrite thin films for magnetic disk media application. *Journal of Alloys and Compounds*, 326(1-2), 215-220.

5. Dias, A.; and Moreira, R.L. (1999). Chemical, mechanical and dielectric properties after sintering of hydrothermal nickel-zinc ferrites. *Materials Letters*, 39(1), 69-76.

6. Salem, M.M.; Panina, L.V.; Trukhanova, E. L.; Darwish, M.A.; Morchenko, A.T.; Zubar, T.I.; Trukhanov, S.V.; and Trukhanov, A.V. (2019). Structural, electric and magnetic properties of $(BaFe_{11.9}Al_{0.1}O_{19})_{1-x}$ - $(BaTiO_3)_x$ composites. *Composites Part B: Engineering*, 174, 107054-107061.

7. Rekaby, M.; Mohammed, N.H.; Ahmed, M.; and Abou-Aly, A.I. (2022). Synthesis, microstructure and indentation Vickers hardness for $(Y_3Fe_5O_{12})_x/Cu_{0.5}Tl_{0.5}Ba_2Ca_2Cu_3O_{10-\delta}$ composites. *Applied Physics A*, 128(4), 261-272.

8. Moitra, D.; Chandel, M.; Ghosh, B.K.; Jani, R.K.; Patra, M.K.; Vadera, S.R.; and Ghosh, N.N. (2016). A simple 'in situ' co-precipitation method for the preparation of multifunctional $CoFe_2O_4$-reduced graphene oxide nanocomposites: excellent microwave absorber and highly efficient magnetically separable recyclable photocatalyst for dye degradation. *RSC Advances,*, 6(80), 76759-76772.

9. Tokunaga, T.; Kaneko, K.; Sato, K.; and Horita, Z. (2008). Microstructure and mechanical properties of aluminum-fullerene composite fabricated by high pressure torsion. *Scripta Materialia*, 58(9), 735-738.

10. Farhat, S.; Rekaby, M.; and Awad, R. (2019). Vickers microhardness and indentation creep studies for erbium-doped ZnO nanoparticles. *SN Applied Sciences,*1(6), 546-557.

11. Joshua, K.J.; Vijay, S.J.; and Selvaraj, D.P. (2018). Effect of nano TiO_2 particles on microhardness and microstructural behavior of AA7068 metal matrix composites. *Ceramics International*, 44(17), 20774-20781.

12. Yassine, M.; El Ghouch, N.; Abdallah, A.M.; Habanjar, K.; and Awad, R. (2022). Structure and magnetic investigation of hard/soft $Ba_{0.5}Sr_{0.5}Fe_{12}O_{19}/x(Ni_{0.5}Zn_{0.5})Fe_2O_4$ nanocomposite. *Journal of Alloys and Compounds*, 907, 164501-164515.

13. Basma, H.; Al Boukhari, J.; Abd Al Nabi, M.; Aridi, A.; Sayed Hasan, R.; Naoufal, D.; Roumie, M.; and Awad, R. (2022). Enhancement of the magnetic and optical properties of $Ni_{0.5}Zn_{0.5}Fe_2O_4$ nanoparticles by ruthenium doping. *Applied Physics A,* 128(5), 409-423.

14. Waldron, R.D. (1955). Infrared spectra of ferrites. *Physical Review*, 99(6), 1727-1735.

15. El-Ghazzawy, E.H. (2020). Effect of heat treatment on structural, magnetic, elastic and optical properties of the co-precipitated $Co_{0.4}Sr_{0.6}Fe_2O_4$. *Journal of Magnetism and Magnetic Materials*, 497, 166017-166027.

16. Singh Yadav, R.; Kuritka, I.; Havlica, J.; Hnatko, M.; Alexander, C.; Masilko, J.; Kalina, L.; Hajducova, M.; and Rusnak, V.E. (2018). Structural, magnetic, elastic, dielectric and electrical properties of hot-press sintered $Co_{1-x}Zn_xFe_2O_4$ (x=0.0, 0.5) spinel ferrite nanoparticles. *Journal of Magnetism and Magnetic Materials*, 447, 48-57.

17. Kumar, S.S.; Singh, R. K.; Verma, P.K.; Siddiqui, M.I.H.; Ali, M.A.; and Manash, A. (2021). Tuning of structural, elastic, luminescence, magnetic, and multiferroic properties of rare earth Ce^{3+} substituted strontium hexaferrite Ceramic magnetic nanomaterials for its industrial applications. *Applied Physics A*, 127(10), 754-765.

18. Mohamed, M.B.; and Wahba, A.M. (2014). Structural, magnetic, and elastic properties of nanocrystalline Al-substituted $Mn_{0.5}Zn_{0.5}Fe_2O_4$ ferrite. *Ceramics International*, 40(8), 11773-11780.

19. Ledbetter, H.M. (1977). Elastic properties of zinc: A compilation and a review. *Journal of Physical and Chemical Reference Data*, 6(4), 1181-1203.

20. Sonu Kumar, S.; Kumar Singh, R.; Kumar, N.; Kumar, G.; and Shankar, U. (2021). Structural, elastic, and multiferroic property of strontium ferrite nanoceramic prepared by sol-gel derived citrate precursor method. *Materials Today: Proceedings*, 46(Part 17), 8567-8572.

21. Ali, I.; Islam, M.U.; Awan, M.S.; Ahmad, M.; Ashiq, M.N.; and Naseem, S. (2013). Effect of Tb^{3+} substitution on the structural and magnetic properties of M-type hexaferrites synthesized by sol-gel auto-combustion technique. *Journal of Alloys and Compounds*, 550, 564-572.

22. El-Ghazzawy, E.H.; and Amer, M.A. (2017). Structural, elastic and magnetic studies of the as-synthesized $Co_{1-x}Sr_xFe_2O_4$ nanoparticles. *Journal of Alloys and Compounds*, 690, 293-303.

23. Raghvendra Singh, Y., Kuřitka, I.; Havlica, J.; Hnatko, M.; Alexander, C.; Masilko, J.; Kalina, L.; Hajdúchová, M.; Rusnak, J.; and Enev, V. (2018). Structural, magnetic, elastic, dielectric and electrical properties of hot-press sintered $Co_{1-x}Zn_xFe_2O_4$ (x=0.0, 0.5) spinel ferrite nanoparticles. *Journal of Magnetism and Magnetic Materials*, 447, 48-57.

24. Leenders, A.; Mich, M.; and Freyhard, H.C. (1997). Influence of thermal cycling on the mechanical properties of VGF melt-textured YBCO. *Physica C: Superconductivity*, 279(3), 173-180.

25. Gong, J.; Wu, J.; and Guan, Z. (1999). Analysis of the indentation size effect on the apparent hardness for ceramics. *Materials Letters*, 38(3), 197-201.

26. Hays, C.; and Kendall, E.G. (1973). An analysis of Knoop microhardness. *Metallography*, 6(4), 275-282.

27. Bull, S.J.; Page, T.F.; and Yoffe, E.H. (1989). An explanation of the indentation size effect in ceramics. *Philosophical Magazine Letters*, 59(6), 281-288.

28. Upit, G.P.; and Varchenya, S.A. (1966). Microhardness of Alkali Halide Crystals. *Physica Status Solidi* (*b*), 17(2), 831-835.

29. Weiss, H. J. (1987). On deriving vickers hardness from penetration depth. *Physica Status Solidi* (*a*), 99(2), 491-501.

30. Li, H.; and Bradt, R.C. (1993). The microhardness indentation load/size effect in rutile and cassiterite single crystals. *Journal of Materials Science*, 28(4), 917-926.

31. Gong, J.; Wu, J.; and Guan, Z. (1999). Examination of the indentation size effect in low-load vickers hardness testing of ceramics. *Journal of the European Ceramic Society*, 19(5), 2625-2631.

32. Khotib, M.; Soegijono, B.; Mas'ud, Z.A.; and Sutriah, K. (2019). Electrocatalytic Properties of Ni-Doped $BaFe_{12}O_{19}$ for Oxygen Evolution in Alkaline Solution. *Open Chemistry*, 17(1), 1382-1392.

33. Vadivelan, S.; and Victor Jaya, N. (2016). Investigation of magnetic and structural properties of copper substituted barium ferrite powder particles via co-precipitation method. *Results in Physics*, 6, 843-850.

34. Ashraf, G.A.; Zhang, L.; Abbas, W.; and Murtaza, G. (2018). Synthesis and characterizations of Al-Sm substituted Ba-Sr M-type hexagonal ferrite nanoparticles via sol-gel route. *Ceramics International*, 44(15), 18678-18685.

35. Thirupathy, C.; Cathrin Lims, S.; John Sundaram, S.; Mahmoud, A.H.; and Kaviyarasu, K. (2020). Equilibrium synthesis and magnetic properties of $BaFe_{12}O_{19}$/$NiFe_2O_4$ nanocomposite prepared by co precipitation method. *Journal of King Saud University - Science*, 32(2), 1612-1618.

36. Muthuselvam, I.P.; and Bhowmik, R.N. (2010). Connectivity between electrical conduction and thermally activated grain size evolution in Ho-doped $CoFe_2O_4$ ferrite. *Journal of Physics D: Applied Physics*, 43(46), 465002-465011.

37. Henaish, A.M.A.; Ali, M.M.; Refaay, D.E.E.; Weinstein, I.A.; and Hemeda, O.M. (2021). Synthesis, electric and magnetic characterization of nickel ferrite/PANI nano-composite prepared by flash auto combustion method. *Journal of Inorganic and Organometallic Polymers and Materials*, 31(2), 731-740.

38. Amer, M.A.; Meaz, T.M.; Attalah, S.S.; and Ghoneim, A.I. (2015). Structural phase transformation of as-prepared Mg-Mn nanoferrites by annealing temperature. *Materials Characterization*, 110, 197-207.

39. Mazen, S.A.; Mansour, S.F.; Dhahri, E.; Zaki, H.M.; and Elmosalami, T.A. (2009). The infrared absorption and dielectric properties of Li-Ga ferrite. *Journal of Alloys and Compounds*, 470(1-2), 294-300.

40. H. Kadam, R.; Borade, R.B.; Mane, M.L.; Mane, D.R.; Batoo, K.M.; and Shirsath, S.E. (2020). Structural, mechanical, dielectric properties and magnetic interactions in Dy^{3+} -substituted Co-Cu-Zn nanoferrites. *RSC Advances*, 10(47), 27911-27922.

41. Ali, I., Islam; M.U., Awan, M.S.; and Ahmad, M. (2013). Effects of Ga-Cr substitution on structural and magnetic properties of hexaferrite ($BaFe_{12}O_{19}$) synthesized by sol-gel auto-combustion route. *Journal of Alloys and Compounds*, 547, 118-125.

42. Ravinder, D. (1994). Composition dependence of the elastic moduli of mixed lithium-cadmium ferrites. *Journal of Applied Physics*, 75(10), 6121-6123.

43. Patange, S.M.; Shirsath, S.E.; Lohar, K.S.; Algude, S.G.; Kamble, S.R.; Kulkarni, N.; Mane, D.R.; and Jadhav, K.M. (2013). Infrared spectral and elastic moduli study of $NiFe_{2-x}Cr_xO_4$ nanocrystalline ferrites. *Journal of Magnetism and Magnetic Materials*, 325, 107-111.

44. Amer, M.A.; Meaz, T.M.; Attalah, S.S.; and Ghoneim, A.I. (2015). Structural phase transition of as-synthesized Sr-Mn nanoferrites by annealing temperature. *Journal of Magnetism and Magnetic Materials*, 393, 467-478.

45. Basfer, N.M.; Mansour, S.F.; and Al-Hazmi, F. (2020). The influence of Cu^{2+} substitution on theoretical and experimental magneto-mechanical properties of Mg-Zn nanoferrites. *Journal of Materials Science: Materials in Electronics*, 31(13), 10889-10902.

46. Barakat, M.ME. (2017). Influence of $Co_{0.5}Zn_{0.5}Fe_2O_4$ Nanoparticles Addition on Vickers Microhardness for $Cu_{0.5}Tl_{0.5}$-1223 Phase. *Journal of Superconductivity and Novel Magnetism*, 30(10), 2945-2955.

47. Xu, L.Y.; Zhang, S.T.; Jing, H.Y.; Wang, L.X.; Wei, J.; Kong, X.C.; and Han, Y.D. (2018). Indentation size effect on ag nanoparticle-modified graphene/Sn-Ag-Cu solders. *Journal of Electronic Materials,* 47(1), 612-619.

48. Costin, W.L.; Lavigne, O.; and Kotousov, A. (2016). A study on the relationship between microstructure and mechanical properties of acicular ferrite and upper bainite. *Materials Science and Engineering: A*, 663, 193-203.

49. Lloyd, D.J. (1994). Particle reinforced aluminium and magnesium matrix composites. *International Materials Reviews*, 39(1), 1-23.

50. Ahmad, I.; Bashir, M.; Sadaqat, A.; Riaz, S.; and Naseem, S. (2015). Effects of temperature on zirconia nanoparticles during and after synthesis. *Materials Today: Proceedings,* 2(10), 5786-5792.

51. Majzoobi, G.H.; Rahmani, K.; and Atrian, A. (2018). Temperature effect on mechanical and tribological characterization of Mg-SiC nanocomposite fabricated by high rate compaction. *Materials Research Express*, 5(1), 015046.

52. Iwaoka, T.; and Nakamura, M. (2011). Effect of compaction temperature on sinterability of magnesium and aluminum powder mixtures by warm compaction method. *Materials Transactions*, 52(5), 943-947.

53. Caldeira, L.E.; Guaglianoni, W.C.; Venturini, J.; Arcaro, S.; Bergmann, C.P.; Braganca, S.R. (2020). Sintering-dependent mechanical and magnetic properties of spinel cobalt ferrite ($CoFe_2O_4$) ceramics prepared via sol-gel synthesis. *Ceramics International*, 46(2), 2465-2472.